

# A finite element method for solving the shallow water equations on the sphere

Richard Comblen <sup>a,\*</sup>, Sébastien Legrand <sup>b</sup>,  
Eric Deleersnijder <sup>a</sup>, Vincent Legat <sup>a</sup>

<sup>a</sup> *Centre for Systems Engineering and Applied Mechanics, Université catholique de Louvain, 4 Avenue Georges Lemaître, B-1348 Louvain-la-Neuve, Belgium*

<sup>b</sup> *Management Unit of the North Sea Mathematical Models, Royal Belgian Institute of Natural Sciences, 100 Gulledele, B-1200 Brussels, Belgium*

---

## Abstract

Within the framework of ocean general circulation modeling, the present paper describes an efficient way to discretize partial differential equations on curved surfaces by means of the finite element method on triangular meshes. Our approach benefits from the inherent flexibility of the finite element method. The key idea consists in a dialog between a local coordinate system defined for each element in which integration takes place, and a nodal coordinate system in which all local contributions related to a vectorial degree of freedom are assembled. Since each element of the mesh and each degree of freedom are treated in the same way, the so-called pole singularity issue is fully circumvented.

Applied to the shallow water equations expressed in primitive variables, this new approach has been validated against the standard test set defined by Williamson et al. (1992). Optimal rates of convergence for the  $P_1^{NC} - P_1$  finite element pair are obtained, for both global and local quantities of interest.

Finally, the approach can be extended to three-dimensional thin-layer flows in a straightforward manner.

*Key words:* curved manifolds, finite element, shallow water equations, spherical geometry

---

---

\* Corresponding author. Tel.: +32 10 47 23 62; fax: +32 10 47 21 80.  
*Email address:* richard.comblen@uclouvain.be (Richard Comblen).

# 1 Introduction

As the shape of Earth is almost spherical, it is critical for atmosphere and ocean modeling to develop efficient methods to solve partial differential equations on the sphere. On the latter, the most intuitive way to discretize a system of equations is to use spherical coordinates. Unfortunately, this coordinate system introduces two singular points, i.e. the poles. At these poles, the North and East directions are undefined and the metric is singular. Those issues need to be addressed, for the purposes of geophysical flow modeling.

We focus on the shallow water equations. Indeed, this two-dimensional model is a key building block for the dynamical core of ocean models. The horizontal momentum equation for a hydrostatic three-dimensional model is rather similar to the momentum part of the shallow water equations. Further, a classical approach in large scale ocean modeling is to resort to mode splitting. The idea of mode splitting is to use a different time stepping for the two-dimensional barotropic mode, whose fastest processes are external gravity waves, and the much slower three-dimensional baroclinic mode, whose fastest processes are internal waves and advection (Gadd, 1978; Madala, 1981; Blumberg and Mellor, 1987; Killworth et al., 1991; Deleersnijder and Campin, 1995; Hallberg, 1997; Higdon and de Szoeke, 1997; Higdon, 2002). In this case, the barotropic mode equations are the shallow water equations, with some additional coupling terms. This is why the shallow water equations are a relevant benchmark.

The pole problem is an issue that has been addressed in many ways:

- In classical longitude-latitude models, the solution can be filtered, the noise near the pole being removed, and the constraint on the time step being weakened (Murray and Reason, 2002).
- The spectral transform method applied to the equations rewritten with vorticity and divergence as prognostic variables rather than the two velocity components is a popular solution to the “pole problem” in atmospheric sciences. Swarztrauber (1996) reviews these methods. The absence of vector field, combined with the calculation of derivatives in spectral space, allows them to be exempt of pole problems. This approach cannot be applied in complex geometry. Hence, it is unlikely to become popular in ocean modeling.
- The use of a scalar expression of the momentum equation such as vorticity-divergence or streamfunction-velocity potential formulations, combined with an expression of the spatial operators in terms of a stencil circumvents the pole problem. Such a formulation using the icosahedral-hexahedral grid can be found in Sadourny et al. (1968); Heikes and Randall (1995); Thuburn (1997). For a model in primitive variables, Majewski et al. (2002) use a local spherical coordinate system at each gridpoint. The latter approach can

be seen as a finite-difference counterpart of the present work.

- A lot of implementations use a single global cartesian coordinate system. Therefore, velocity vectors are expressed with three components rather than two. These additional degrees of freedom are either deduced from the other d.o.f. (Priestley, 1992) or constrained by a Lagrange multiplier (Côté, 1988), ensuring that velocity vectors remain tangent to the surface of the sphere (Swarztrauber et al., 1997; Stuhne and Peltier, 1999; Giraldo, 2000; Tomita et al., 2001; Giraldo et al., 2002, 2003; Giraldo and Warburton, 2005; Giraldo, 2006). Further, Stuhne and Peltier (2006) applied this approach to three-dimensional oceanic flows in the framework of finite volume schemes.
- Splitting the sphere into several domains, each having its own curvilinear coordinate system appears as an attractive approach. The “cubed sphere” with six local curvilinear coordinate systems is introduced in several papers (Ronchi et al., 1996; Taylor et al., 1997; Adcroft et al., 2004; Nair et al., 2005; Rossmanith, 2006; St-Cyr et al., 2008). A spherical coordinate system, with two stereographic caps at the poles is also used in atmosphere modeling (Lanser et al., 2000). Ocean modelers use several spherical coordinate systems, for instance one rotated for the North-Atlantic and the Arctic Oceans, in addition to the classical one (Deleersnijder et al., 1993; Eby and Holloway, 1994; Coward et al., 1994; Webb et al., 1998).
- Finally, stretched or multipolar grids are often used in oceanography, with the poles located on dry land (Murray, 1996; Madec and Imbard, 1996; Roberts et al., 2006). This methodology is efficient for the world ocean, but cannot be used for simulating atmospheres or truly global oceans (aquaplanets) such as that of Europa, the moon of Jupiter.

In this paper, an efficient approach to handle partial differential equations on the sphere is developed for global ocean modeling. Our technique provides a good compromise between simplicity, efficiency and accuracy. It has been successfully applied in the development of SLIM (**S**econd-generation **L**ouvain-la-Neuve **I**ce-Ocean **M**odel - <http://www.climate.be/SLIM>). As all general circulation models, it uses primitive variables as prognostic quantities. We take advantage of the inherent geometrical flexibility of the finite element method to generalize the geometrical algorithm to any smooth manifold. The extension of this method to three-dimensional thin-layer flows is straightforward. In addition, the method only implies a few modifications in the finite element algorithm, and allows us to use the same model for both planar and curvilinear problems. Finally, the computational overhead to handle the spherical geometry is almost negligible.

The paper is organized as follows. Section 2 describes the methodology for dealing with curved geometry. Section 3 is devoted to the validation of the method on the test cases of Williamson et al. (1992). Finally, section 4 shows how our finite element scheme behaves for the difficult test case of Smith and Dritschel (2006).

## 2 An efficient methodology to handle PDEs in spherical geometry

The inviscid shallow water equations can be obtained by averaging the incompressible Navier-Stokes equations along the vertical direction. The usual non-conservative form reads:

$$\frac{\partial \mathbf{u}}{\partial t} + \mathbf{u} \cdot \nabla \mathbf{u} + f \mathbf{k} \times \mathbf{u} + g \nabla \eta = 0, \quad (1)$$

$$\frac{\partial \eta}{\partial t} + \nabla \cdot [(h + \eta) \mathbf{u}] = 0, \quad (2)$$

where  $\mathbf{u}$  is the two-dimensional mean velocity,  $\eta$  is the elevation of the free-surface,  $f$  is the Coriolis parameter,  $\mathbf{k}$  is a unit upward normal vector,  $g$  is the gravitational acceleration and  $h$  is the reference depth at rest.

Unlike finite differences, the finite element method does not need a global coordinate system to derive the discrete matrix operators. If the most obvious discrete finite difference differential operators on the sphere are directly built along meridians and parallels, the finite element local matrices, that define the local discrete differential operators, are usually built in the framework of a local coordinate system defined for each element. In other words, the finite elements intrinsically do not exhibit the classical coordinates singularity issue. The basic principle adopted herein is to write local problems in a local orthonormal curvilinear system  $(\mathbf{e}_\xi, \mathbf{e}_\eta, \mathbf{e}_\zeta)$  defined for each element. Both  $\mathbf{e}_\xi$  and  $\mathbf{e}_\eta$  are tangent to the surface of the sphere, while the normal to the surface is given by  $\mathbf{e}_\zeta$ . The next step consists in assembling all the local problems in the global discrete algebraic system. As the local vectorial equations are written in distinct coordinate systems, it is required to perform suitable change of variables to rewrite the local contributions in the same coordinate system. As we cannot use a single coordinate system valid for each point on the sphere, we define a nodal orthonormal coordinate system  $(\mathbf{e}_x, \mathbf{e}_y, \mathbf{e}_z)$  associated with each vectorial degree of freedom,  $\mathbf{e}_x$  and  $\mathbf{e}_y$  being tangent to the surface. A key advantage of the finite elements is that the support of a shape function is limited to only a few elements. Then, this nodal coordinate system needs to be valid only on the elements where the associated shape function does not vanish. Finally, a global reference system is needed only to define the position of the vertices and the components of both local and nodal basis vectors.

Basically, the pole problem arises when a vectorial equation of a vectorial quantity has to be solved. For notational convenience, we highlight the most important aspects on a simplified case, without any loss of generality. For instance, let us only consider the resolution of the momentum equation (1) of the shallow water model on the sphere. Equation (1) can be written in the following compact notation:

$$\mathbf{f}(\mathbf{u}) = 0, \quad (3)$$

where the vector  $\mathbf{u}$  tangent to the surface is expressed in terms of local or nodal components:

$$\mathbf{u} = u^\xi \mathbf{e}_\xi + u^\eta \mathbf{e}_\eta = u^x \mathbf{e}_x + u^y \mathbf{e}_y. \quad (4)$$

In order to switch from the local to the nodal basis, a local linear operator is defined such as:

$$\underbrace{\begin{pmatrix} u^x \\ u^y \end{pmatrix}}_{x\mathbf{U}} = \underbrace{\begin{pmatrix} \mathbf{e}_x \cdot \mathbf{e}_\xi & \mathbf{e}_x \cdot \mathbf{e}_\eta \\ \mathbf{e}_y \cdot \mathbf{e}_\xi & \mathbf{e}_y \cdot \mathbf{e}_\eta \end{pmatrix}}_{x\mathbf{P}_\xi} \underbrace{\begin{pmatrix} u^\xi \\ u^\eta \end{pmatrix}}_{\xi\mathbf{U}}. \quad (5)$$

Conversely, the transformation from the nodal to the local basis is defined by:

$$\underbrace{\begin{pmatrix} u^\xi \\ u^\eta \end{pmatrix}}_{\xi\mathbf{U}} = \underbrace{\begin{pmatrix} \mathbf{e}_\xi \cdot \mathbf{e}_x & \mathbf{e}_\xi \cdot \mathbf{e}_y \\ \mathbf{e}_\eta \cdot \mathbf{e}_x & \mathbf{e}_\eta \cdot \mathbf{e}_y \end{pmatrix}}_{\xi\mathbf{P}_x} \underbrace{\begin{pmatrix} u^x \\ u^y \end{pmatrix}}_{x\mathbf{U}}. \quad (6)$$

If both systems are orthonormal curvilinear representations of the same  $\mathcal{C}_1$  surface, the matrix  $x\mathbf{P}_\xi$  is the inverse of  $\xi\mathbf{P}_x$ .

In order to solve the nonlinear equation (1), it is common to have recourse to standard linearization techniques, such as the Newton-Raphson method:

$$\mathbf{A}\mathbf{u} = \mathbf{b}, \quad (7)$$

where  $\mathbf{A}$  is the gradient of  $\mathbf{f}$  (or a suitable approximation of this gradient). Equation (7) may be viewed in terms of local components inside each element:

$$\underbrace{\begin{pmatrix} a_{\xi\xi} & a_{\xi\eta} \\ a_{\eta\xi} & a_{\xi\xi} \end{pmatrix}}_{\xi\mathbf{A}_\xi} \underbrace{\begin{pmatrix} u^\xi \\ u^\eta \end{pmatrix}}_{\xi\mathbf{U}} = \underbrace{\begin{pmatrix} b_\xi \\ b_\eta \end{pmatrix}}_{\xi\mathbf{B}}. \quad (8)$$

The same equation can also be expressed in terms of nodal components:

$$\underbrace{\begin{pmatrix} a_{xx} & a_{xy} \\ a_{yx} & a_{yy} \end{pmatrix}}_{x\mathbf{A}_x} \underbrace{\begin{pmatrix} u^x \\ u^y \end{pmatrix}}_{x\mathbf{U}} = \underbrace{\begin{pmatrix} b_x \\ b_y \end{pmatrix}}_{x\mathbf{B}}. \quad (9)$$

To assemble local contributions (8) into a common nodal version, it is required to transform equation (8) into equation (9). Such a transformation can be obtained easily by matrix operations, taking advantage of the relations (5-6):

$$\begin{array}{ccc} \xi\mathbf{A}_\xi & \xi\mathbf{U} & = \xi\mathbf{B} \\ & \downarrow & \\ \xi\mathbf{A}_\xi & \underbrace{\xi\mathbf{P}_x}_{x\mathbf{P}_\xi} \xi\mathbf{U} & = \xi\mathbf{B} \\ \underbrace{x\mathbf{P}_\xi}_{x\mathbf{P}_\xi} \xi\mathbf{A}_\xi \underbrace{\xi\mathbf{P}_x}_{x\mathbf{P}_\xi} & \xi\mathbf{U} & = \underbrace{x\mathbf{P}_\xi}_{x\mathbf{P}_\xi} \xi\mathbf{B} \\ & \downarrow & \\ x\mathbf{A}_x & x\mathbf{U} & = x\mathbf{B}. \end{array}$$

## 2.1 Finite element formulation

To obtain a discrete algebraic system, it is required to define a piecewise polynomial approximation of the unknown field. In the local basis, such an approximation can be written as the linear combination of  $n$  local shape functions:

$$\xi\mathbf{U} \simeq \sum_{i=1}^n \phi_i(\xi, \eta) \underbrace{\begin{pmatrix} \xi U_i \\ \eta U_i \end{pmatrix}}_{\xi\mathbf{U}_i^h}. \quad (10)$$

On each element, a weak formulation of (8) can be derived through the Galerkin procedure (Hughes, 2000):

$$\xi\mathbf{A}_\xi^h \xi\mathbf{U}^h = \xi\mathbf{B}^h, \quad (11)$$

where  $\xi\mathbf{U}^h = [\xi U_1 \ \eta U_1 \ \xi U_2 \ \eta U_2 \ \dots \ \xi U_n \ \eta U_n]^T$ . For simplicity, let us restrict ourself to Turner triangles (linear conforming  $P_1$  elements). In this case, only three nodes exist. The length of  $\xi\mathbf{U}^h$  and  $\xi\mathbf{B}^h$  is 6, and the size of the matrix

${}_{\xi}\mathbf{A}_{\xi}^h$  is  $6 \times 6$ . To obtain the global algebraic system, equation (11) must be expressed in terms of the nodal components:

$$\begin{array}{ccc}
{}_{\xi}\mathbf{A}_{\xi}^h & {}_{\xi}\mathbf{U}^h & = & {}_{\xi}\mathbf{B}^h \\
\downarrow & & & \\
{}_{\xi}\mathbf{A}_{\xi}^h & \overbrace{{}_{\xi}\mathbf{P}_x^h} & {}_{\xi}\mathbf{U}^h & = & {}_{\xi}\mathbf{B}^h \\
\overbrace{{}_x\mathbf{P}_{\xi}^h} & \underbrace{{}_{\xi}\mathbf{A}_{\xi}^h} & \underbrace{{}_{\xi}\mathbf{P}_x^h} & {}_x\mathbf{U}^h & = & \underbrace{{}_x\mathbf{P}_{\xi}^h} & \underbrace{{}_{\xi}\mathbf{B}^h} \\
\downarrow & & & & & \downarrow \\
{}_x\mathbf{A}_x^h & & {}_x\mathbf{U}^h & = & & {}_x\mathbf{B}^h,
\end{array} \tag{12}$$

where the transformation operator is now given by:

$${}_{\xi}\mathbf{P}_x^h = \begin{pmatrix} | & & | \\ \xi\mathbf{P}_{x_1} & & \\ | & & | \\ \hline & \xi\mathbf{P}_{x_2} & \\ \hline & & \xi\mathbf{P}_{x_3} \\ | & & | \end{pmatrix}. \tag{13}$$

The symbol  $\xi\mathbf{P}_{x_i}$  denotes the transformation operator from the local basis of the element onto the nodal basis associated to the  $i^{\text{th}}$  node of this element. Then the usual assembling procedure of the finite element method can be applied.

To consider the general coupled shallow water equations, we just need to define  ${}_{\xi}\mathbf{U}^h$  and  ${}_{\xi}\mathbf{P}_x^h$  as follows:

$${}_{\xi}\mathbf{U}^h = \begin{pmatrix} \xi\mathbf{U}_1^h \\ \hline E_1 \\ \xi\mathbf{U}_2^h \\ \hline E_2 \\ \xi\mathbf{U}_3^h \\ \hline E_3 \end{pmatrix}, \quad {}_{\xi}\mathbf{P}_x^h = \begin{pmatrix} | & & | \\ \xi\mathbf{P}_{x_1} & & \\ | & & | \\ \hline & 1 & \\ \hline & \xi\mathbf{P}_{x_2} & \\ \hline & & 1 \\ \hline & & \xi\mathbf{P}_{x_3} \\ | & & | \\ & & 1 \end{pmatrix}, \tag{14}$$

where  $E_i$  denote the nodal values of elevation. The diagonal terms equal to unity corresponds to the elevation degrees of freedom.

## 2.2 Selection of the mapping

To obtain the discrete algorithm, we have to choose a local curvilinear coordinate system. The available choices range from the exact discretization of the surface (spherical triangles) to linear mapping (flat triangles). On the one hand, the spatial differential operators for spherical triangles must take into account the variations of the local basis vectors, as the mapping is nonlinear. These complex expressions can be derived with the help of differential geometry theory. An accurate quadrature rule has to be introduced to integrate the nonlinearities due to the mapping. On the other hand, flat triangles allows us to use the classical cartesian expressions of differential operators, and low order quadrature rules are sufficient.

The geometrical error with flat triangles converge at the same rate as the discretization error when linear interpolations are used. Typically, the derivatives of the velocity field with respect to the local variables are:

$$\frac{\partial \mathbf{u}}{\partial \xi} = \left( \frac{\partial u^\xi}{\partial \xi} + \Gamma_{\xi\xi}^\xi u^\xi + \Gamma_{\xi\eta}^\xi u^\eta \right) \mathbf{e}_\xi + \left( \frac{\partial u^\eta}{\partial \xi} + \Gamma_{\xi\xi}^\eta u^\xi + \Gamma_{\xi\eta}^\eta u^\eta \right) \mathbf{e}_\eta, \quad (15)$$

$$\frac{\partial \mathbf{u}}{\partial \eta} = \left( \frac{\partial u^\xi}{\partial \eta} + \Gamma_{\eta\xi}^\xi u^\xi + \Gamma_{\eta\eta}^\xi u^\eta \right) \mathbf{e}_\xi + \left( \frac{\partial u^\eta}{\partial \eta} + \Gamma_{\eta\xi}^\eta u^\xi + \Gamma_{\eta\eta}^\eta u^\eta \right) \mathbf{e}_\eta, \quad (16)$$

where  $\Gamma_{\beta\gamma}^\alpha$  are the second kind Christoffel symbols. In Appendix A, we show that those symbols scale as:

$$\Gamma_{\beta\gamma}^\alpha \approx \frac{h}{r^2}, \quad (17)$$

with  $r$  the radius of the sphere (or the local radius of curvature for a more complex manifold), and  $h$  the length of the largest edge. Inspecting the orders of magnitude of the coefficients in the discretized version of equations (15-16), we get:

$$\begin{aligned} \frac{\partial \mathbf{u}}{\partial \xi} &\approx \left( \frac{u_{i+1,j}^\xi - u_{i-1,j}^\xi}{2h} + \mathcal{O}\left(\frac{h}{r^2}\right) u_{i,j}^\xi + \mathcal{O}\left(\frac{h}{r^2}\right) u_{i,j}^\eta \right) \mathbf{e}_\xi + (\dots) \mathbf{e}_\eta \\ &\approx \frac{1}{h} \left( \frac{u_{i+1,j}^\xi - u_{i-1,j}^\xi}{2} + \mathcal{O}\left(\frac{h^2}{r^2}\right) u_{i,j}^\xi + \mathcal{O}\left(\frac{h^2}{r^2}\right) u_{i,j}^\eta \right) \mathbf{e}_\xi + (\dots) \mathbf{e}_\eta. \end{aligned} \quad (18)$$

Thus, in the discrete system, when flat triangles are used, the ratio between the curvature terms and the dominant terms is of order  $h^2/r^2$ . This means

that, in the case of flat triangles, where such curvature terms disappears, the geometrical errors will converge with a quadratic rate, as the discretization error for linear finite elements. Moreover, as long as  $r \gg h$ , this geometrical error will be much smaller than the discretization one. In ocean modeling, the sizes of all elements are always tiny in comparison to Earth radius. Therefore, when linear finite element are used, flat triangles are sufficient.

For vectorial degrees of freedom defined at nodes, it is now impossible to define a nodal coordinate system that is coplanar to all local coordinate systems of neighboring triangles. The most natural definition of the nodal basis located at a vertex consists in taking  $\mathbf{e}_z$  as a weighted average of the normals of the surrounding elements, while the two other axes are chosen arbitrarily. This is the classical definition of the normal to a mesh at a node (Gresho and Sani, 2000, p. 542). The transfer operator  ${}_x\mathbf{P}_\xi$  can be defined by equation (5). The converse transfer operator  ${}_\xi\mathbf{P}_x$  defined by equation (6) is not  $({}_x\mathbf{P}_\xi)^{-1}$  anymore. To ensure consistency,  ${}_x\mathbf{P}_\xi {}_\xi\mathbf{P}_x$  should be the identity operator, so we define  ${}_\xi\mathbf{P}_x = ({}_x\mathbf{P}_\xi)^{-1}$ .

For vectorial degrees of freedom defined along the edges, it exists a natural definition of  ${}_x\mathbf{P}_\xi$ . The two triangles sharing a common edge can be unfolded onto a plane. The nodal basis on the edge is defined so that  $\mathbf{e}_x$  axis is aligned with the edge, and  $\mathbf{e}_y$  axis is embedded in the plane. Then the transfer matrices between any of these bases are simply two-dimensional rotation matrices. Then the following property holds:  ${}_x\mathbf{P}_\xi^{-1} = {}_x\mathbf{P}_\xi^T = {}_\xi\mathbf{P}_x$ .

To sum up, a simple general methodology to handle curved geometry has been developed. It can be implemented into standard flat geometry softwares with only marginal modifications. The whole geometry is fully defined by the discrete vertices of the mesh. Therefore, such a methodology is valid for any manifold discretized by the vertices. It must be emphasized that all triangles will be handled in the same way. As a consequence, the pole problem is completely circumvented. The computational overhead is very small, since only local matrix/matrix and matrix/vector multiplications are added, as explained in equation (12). All the conservation properties of the discretization are preserved.

### 3 Validation with the shallow water equations

The methodology developed above is validated using the  $P_1^{NC} - P_1$  discretization, applied to the shallow water equations. The non-conforming linear shape functions  $P_1^{NC}$  for velocities, and conforming linear ones  $P_1$  for elevation are illustrated in figure 1. The velocity nodes are located at the mid-edge points, and the elevation ones on the vertices. This pair of elements is well suited for

shallow water flows (Hanert et al., 2005). It enjoys attractive mathematical properties in terms of spurious elevation modes, that could appear in a mixed discretization of the steady state shallow water equations (Le Roux et al., 2005; Hanert and Legat, 2006). In addition, the shape functions for velocities are orthogonal, so the blocks of the mass matrix corresponding to the velocities are diagonal. It is particularly advantageous for an explicit time integration, without any mass lumping. The linear system is nondiagonal only for elevation nodes, which account only a seventh of the whole set of degrees of freedom. As the nonconforming linear shape functions are discontinuous on the edges, this approximation can be viewed as a hybrid choice between continuous and discontinuous approximations. In short, this element seems to combine most advantages of both continuous and discontinuous approaches. On the one hand, the discontinuous character allows us to stabilize the momentum equation with an approximate Riemann solver. On the other hand, sharing the same mid-edge value allow us to implement diffusive second order terms in a straightforward manner (Hanert et al., 2004, 2005).

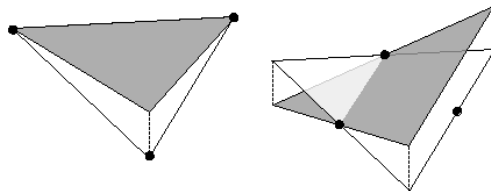


Figure 1. Conforming (left), and non-conforming (right) linear triangular shape functions. The former is used for the elevation, while the latter is resorted to the velocity components.

Within the framework of the SLIM project, the time integration is performed by a family of so-called IMEX Runge-Kutta methods, where the linear terms can be treated implicitly (Ascher et al., 1997). In this case, the time step is only constrained by the usual Courant-Friedrichs-Lewy condition associated with advective terms. In most oceanic flows, such a condition is much less stringent than the stability condition related to the external gravity waves if we use a fully explicit time integrator. The ratio between explicit and semi-implicit time steps is of the order of the Froude number. However, as all the test cases evaluated here are highly advective, the advantage of semi-implicit time-stepping is much smaller. As we want to evaluate the spatial discretization, explicit Runge-Kutta time-stepping schemes have been used, so that the stable time step ensure that the errors due to the time discretization are small.

Five of the seven standard test cases defined by Williamson et al. (1992, hereafter W92) are considered. The two remaining test cases are dropped because implementation of complicated source terms will be needed, or it will involve an initial condition problem for the atmosphere that is of no major interest for ocean modeling. All papers related to the shallow water equations on the

sphere include validation results based on these test cases which can be now viewed as a de facto benchmark. Numerical solutions can be easily compared to analytical ones or to numerical reference results. To perform mesh refinement analysis, we consider four meshes deduced from the icosahedron, where the faces are recursively divided into four triangles and then projected onto the sphere. The meshes shown in figure 2 are made of almost equilateral triangles, with nearly uniform edge length.

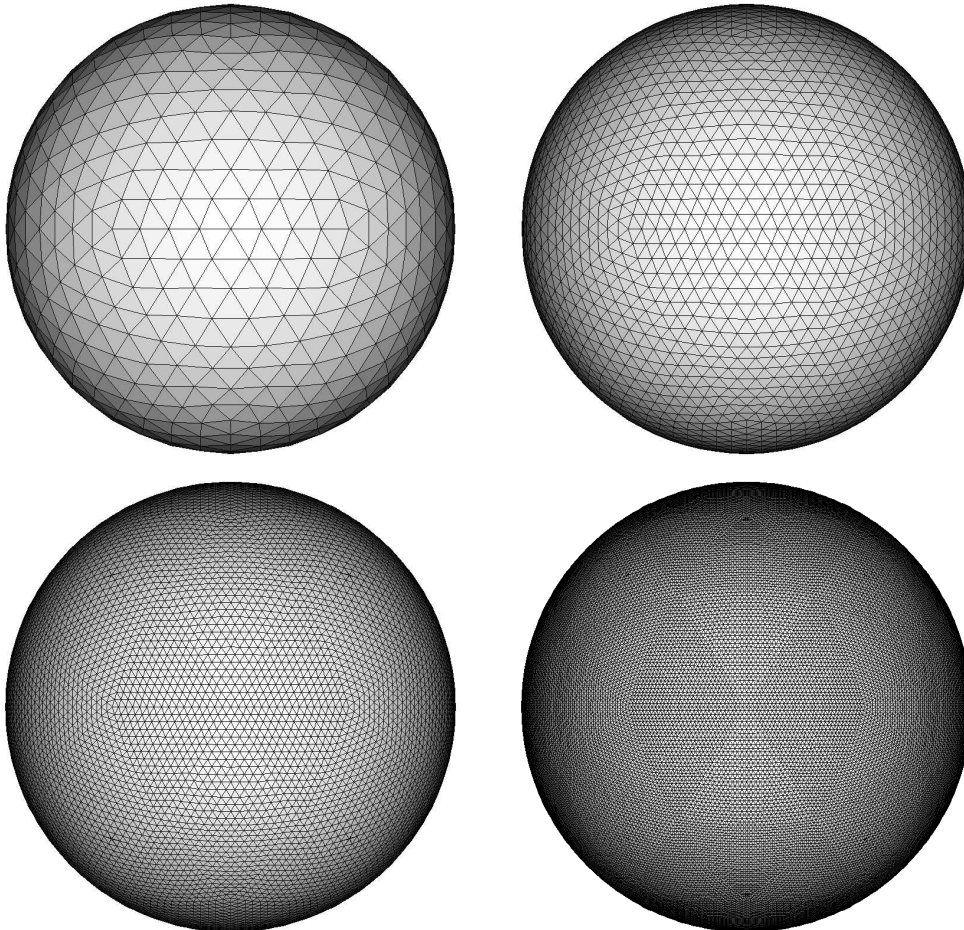


Figure 2. Meshes based upon the icosahedron, with each face recursively refined 3, 4, 5 and 6 times. The number of triangles are respectively 1280, 5120, 20480 and 81920.

### 3.1 *W92 test case 1: advection of a cosine bell of tracer*

Solving accurately the advection of a cosine bell on the sphere is a quite good test of the ability of a numerical scheme to represent efficiently any velocity field, anywhere on the sphere. The advection equation is the equation for elevation (2) with a uniform depth and a nondivergent velocity field constant in time. Using a single spherical coordinate system, the velocity field of this

problem exhibits discontinuities for both North and East component at the poles. The finite element method naturally circumvents this issue. Calculations are performed with an initial tracer field defined as a cosine bell, with values between 0 and 1000. This bell is advected with a constant velocity field corresponding to a solid body rotation. The orientation of the velocity field is tilted of 0.05 radian to avoid any effect of symmetry.  $P_1^{NC}$  elements are used. Advection is stabilized using upwind fluxes, as described in Hanert et al. (2004). The initial condition and the solution obtained after one revolution cannot be distinguished in figure 3. It can also be observed that the  $L_2$  error norm converges at the optimal quadratic rate.

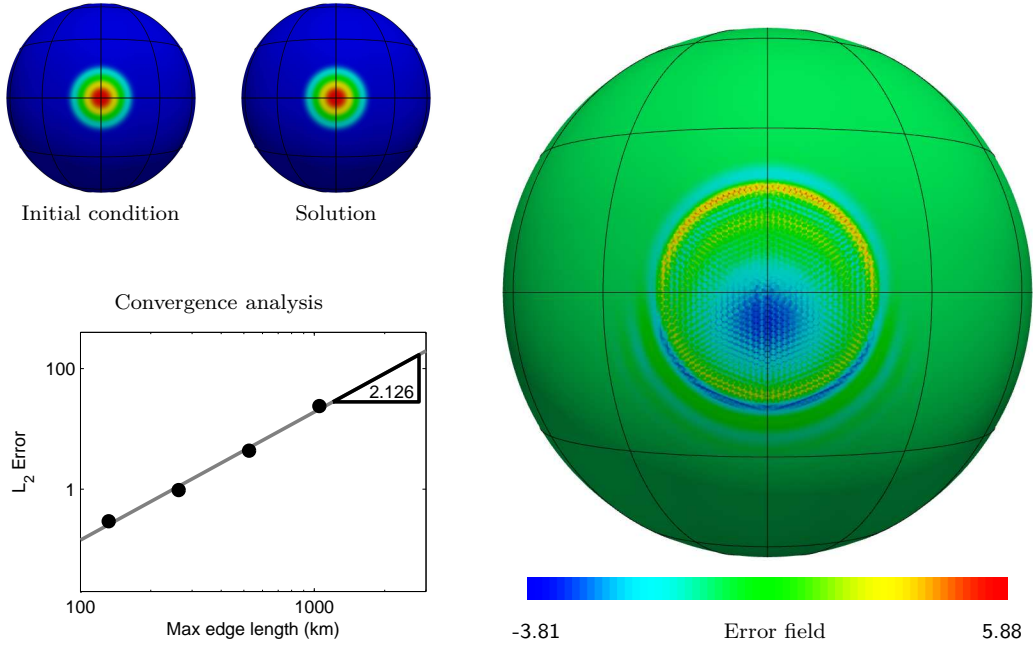


Figure 3. Advection of a cosine bell. Graphical comparison between the initial condition and the numerical solution after one revolution, on a mesh of 81920 triangles (top left). Error distribution on this mesh exhibits small amplitude wiggles (right), and the convergence plot of the  $L_2$  error illustrates the observed quadratic rate of convergence (bottom left).  $L_2$  error is defined as  $\sqrt{\int_{\Omega} (c^h - c)^2 d\Omega / \int_{\Omega} 1 d\Omega}$ .

### 3.2 W92 test cases 2 and 3: zonal geostrophic flows

Williamson's two next benchmarks are steady-state solutions to the nonlinear inviscid shallow water equations. In the first case, the velocity field corresponds to a solid body rotation along the axis of rotation of the Earth, whereas in the second case, it is nonzero only for latitude ranging between 30°South and 90°North. The elevation is defined so that it balances the Coriolis and advection terms of the momentum equation. W92 recommends to compute the error after five physical days. The results of a convergence analysis on

both flows are detailed in figure 4. The optimal rate of convergence for this linear finite element pair in  $L_2$  norm is observed for both elevation and velocity fields.

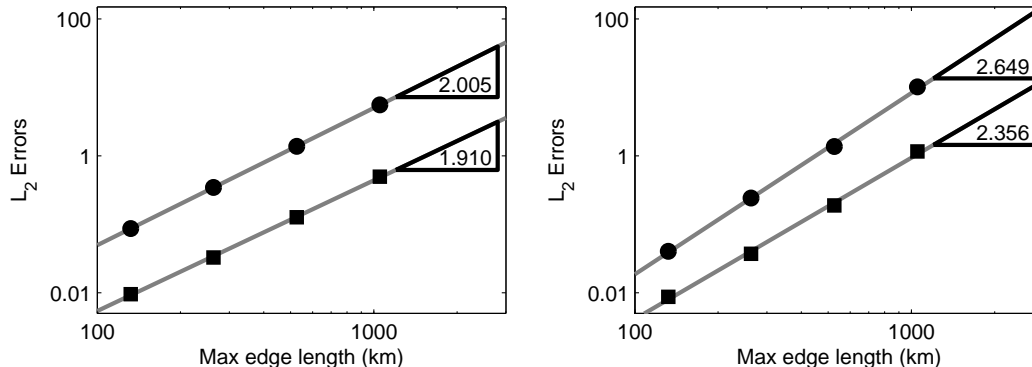


Figure 4. Convergence analysis for test case 2 (left) and test case 3 (right).  $L_2$  error norms on the elevation  $\eta$  (dots) and velocities  $\mathbf{u}$  (squares) after five days of simulation on the different meshes built upon the icosahedron (figure 2).  $L_2$  errors are defined as  $\sqrt{\int_{\Omega} (c^h - c)^2 d\Omega} / \int_{\Omega} 1 d\Omega$ .

### 3.3 W92 test case 5: zonal flow over an isolated mountain

This is the first unsteady test case evaluated. The initial condition is similar to the one of test case 2: a solid body rotation velocity field, with the elevation in geostrophical balance. The only difference is the bathymetry: a seamount conical in the longitude-latitude representation is added, centered on a point with latitude  $30^\circ$ North. The radius of the seamount at its base is  $20^\circ$ , and its height is roughly a third of the fluid mean depth. The flow is going eastward.

In figure 5, our solution is compared to a very high resolution one from the German Weather Service. They simulate this benchmark with a spectral transform shallow water model, based on the NCAR's model (Jakob-Chien et al., 1995) (model truncation: T-426,  $1280 \times 640$  gridpoints, time-step of 90 s)<sup>1</sup>. We use our finest mesh with 81920 triangles. The time step is 90 s. The spectral model has a hyperviscous dissipation term  $\nabla^4$  (with coefficient  $4.97 \times 10^{11}$  m<sup>4</sup>/s), whereas our model does not have any explicit dissipation term, the subgrid-scale features being filtered out by the upwinding of the numerical scheme. The finite element model has 286720 degrees of freedom, while the spectral model has in its grid component more than two million of unknowns. Thus, the spectral solution should be much more resolved than the finite element one.

The difference plots exhibits the Gibbs phenomenon around the mountain,

<sup>1</sup> Data are available at <http://icon.enes.org/swm/stswm/node5.html>

which is specific to spectral methods, and due to the sharp edges of the cone. The amplitude of the difference field is less than one percent of the initial range of elevation. It is believed that the pattern of the difference field is mainly the wiggles due to the spectral method, since this pattern does not change between our two finest meshes, whereas scalar diagnostics do converge. Indeed, figure 6 shows that the maximum and minimum values of elevation converge both at the optimal quadratic rate. Further, the error on the total energy of the system after five days, illustrated in figure 7, converges at an higher rate than expected.

### 3.4 *W92 test case 6: Rossby-Haurwitz waves*

This test case has been widely used for model intercomparison. It consists of slow waves, which are steadily evolving solutions of the nondivergent barotropic vorticity equations (Haurwitz, 1940). The initial patterns of elevation and velocities are shown in figure 8. When this flow was chosen as a test case by W92, it was thought to be stable for the inviscid nonlinear shallow water equations. In fact, Thuburn and Li (2000) showed that it is dynamically unstable, the wave pattern breaking down if initially perturbed.

Figure 9 compares our solution to a reference one. The latter was obtained by the German Weather Service by means of the model that was also used in test case 5, with T-511 resolution (1536x768 grid points), and a 90 s time step. Our model was used with a 60 s time step, on the icosahedral grid refined six times.

As seen in the plots of the right panel, the 4-periodic shape of the difference field evolves toward a 2-periodic shape. This can be understood easily. As explained by Thuburn and Li (2000), the flow is unstable to small perturbations. The spectral method does not trigger this instability because of its high degree of symmetry: truncation errors will always be 4-periodic, since both the grid and the initial condition are 4-periodic. This is why the spectral model keeps the 4-periodic wave pattern so long: only rounding errors excite the instability. The icosahedral mesh is only 2-periodic. Therefore, the truncation errors are 2-periodic. Hence, they excite the 2-periodic component of the unstable mode, which is seen on figure 9. The difference field is an image of the asymmetry of the mesh.

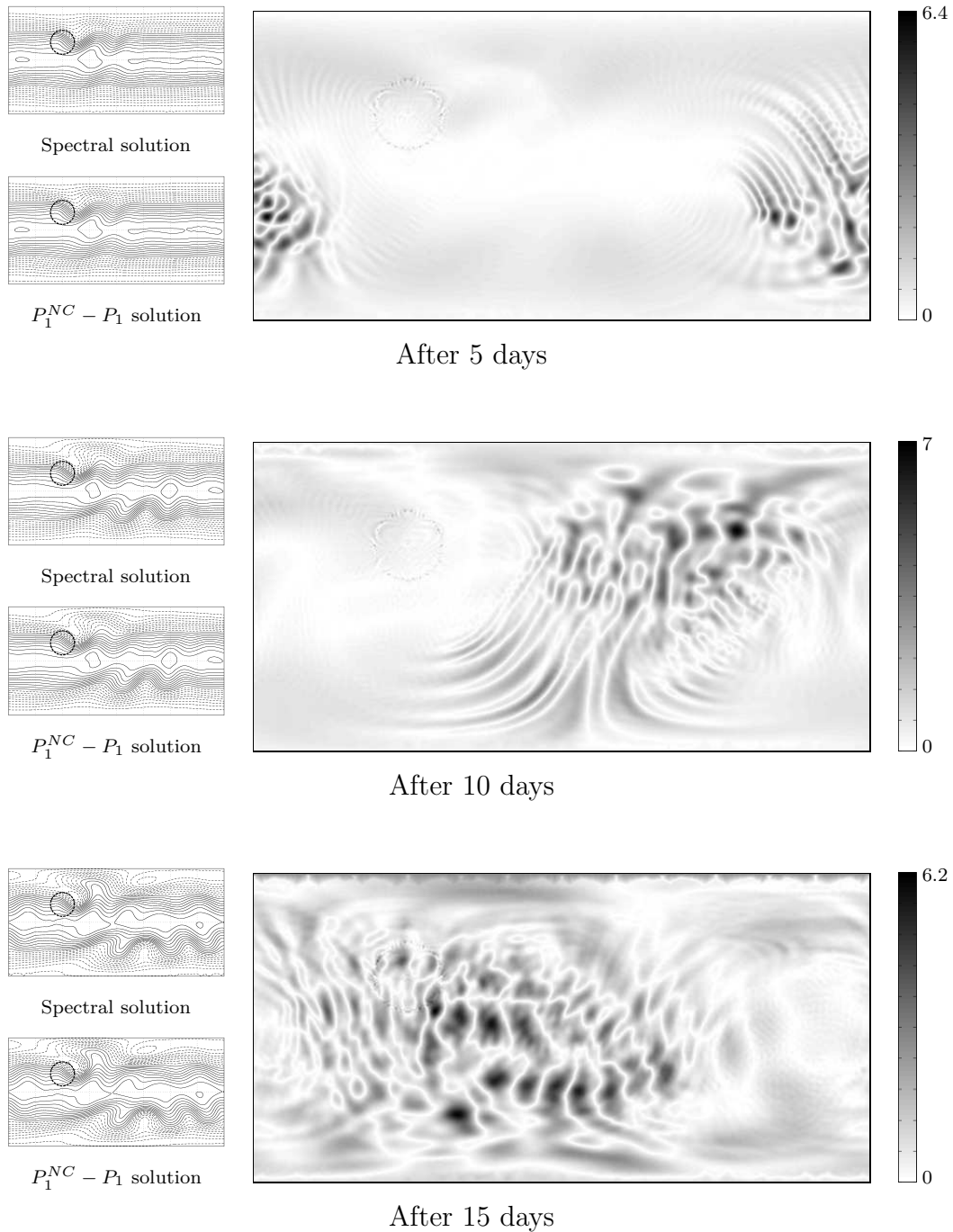


Figure 5. Comparison of the elevation field with reference solution from the German Weather Service for test case 5. The fields are presented in longitude-latitude projection. Left panel: spectral solution on top, and finite element solution on bottom. The interval between contourlines is 50m, the dashed lines are contourlines under the mean level, and the solid lines are contourlines above the mean level. Right panel: visualization of the absolute value of the difference between the reference solution and the finite element solution. The colormaps for the difference range in  $[0; 6.4]$ ,  $[0; 7]$  and  $[0; 6.2]$  (white is 0, black is maximum).

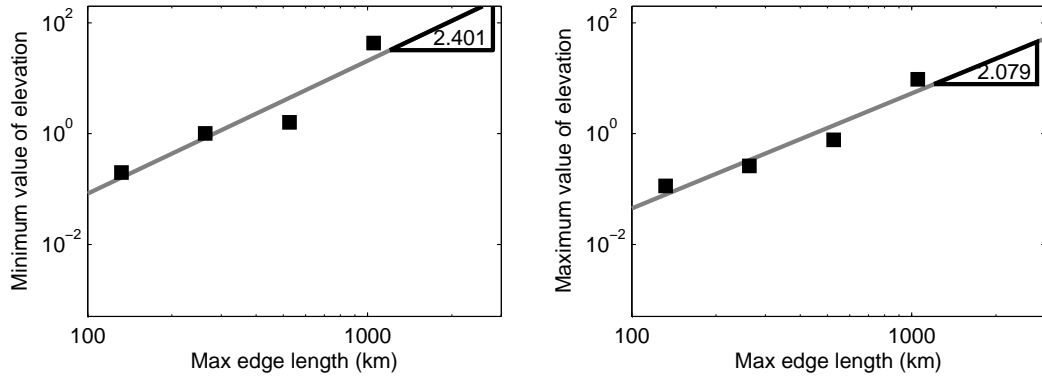


Figure 6. Convergence of the difference between reference solution and finite element solution for minimum (left) and maximum (right) values of elevation for test case 5 of W92.

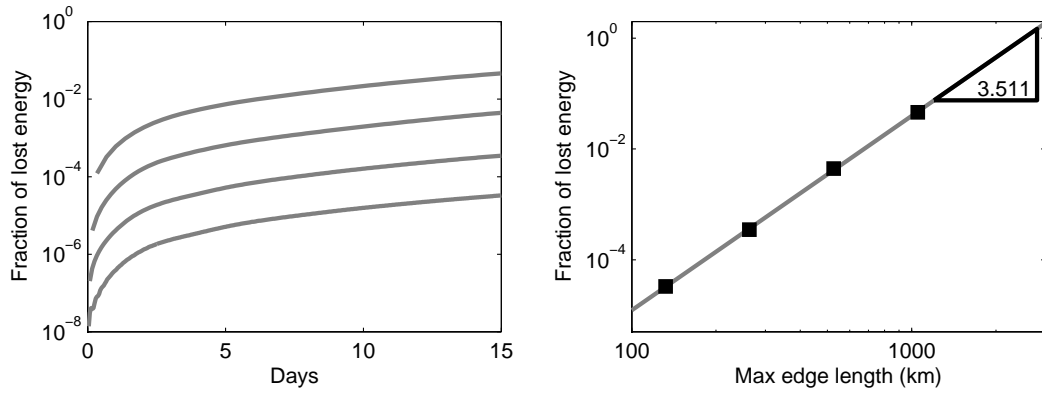


Figure 7. Fraction of total energy lost by the scheme for test case 5 of W92. Left: time series for the four meshes, right: convergence after 15 physical days.

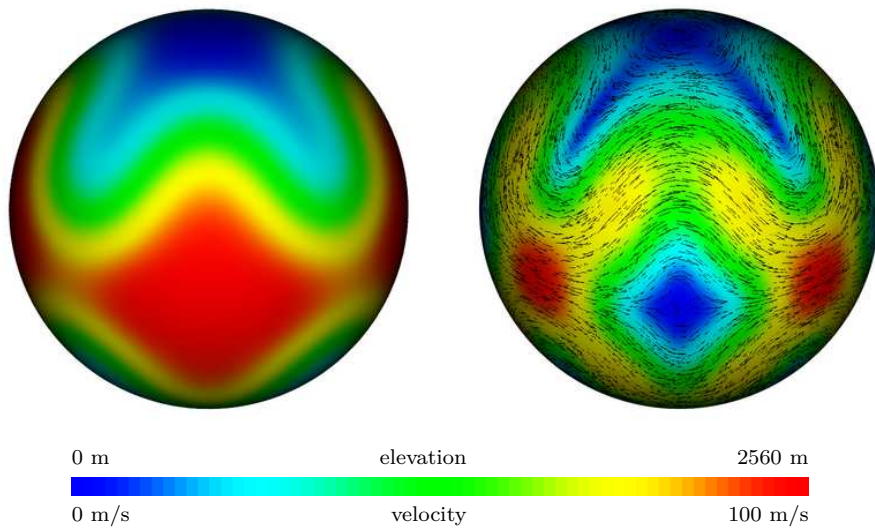


Figure 8. Initial elevation (left) and velocity (right) fields for test case 6 of W92.

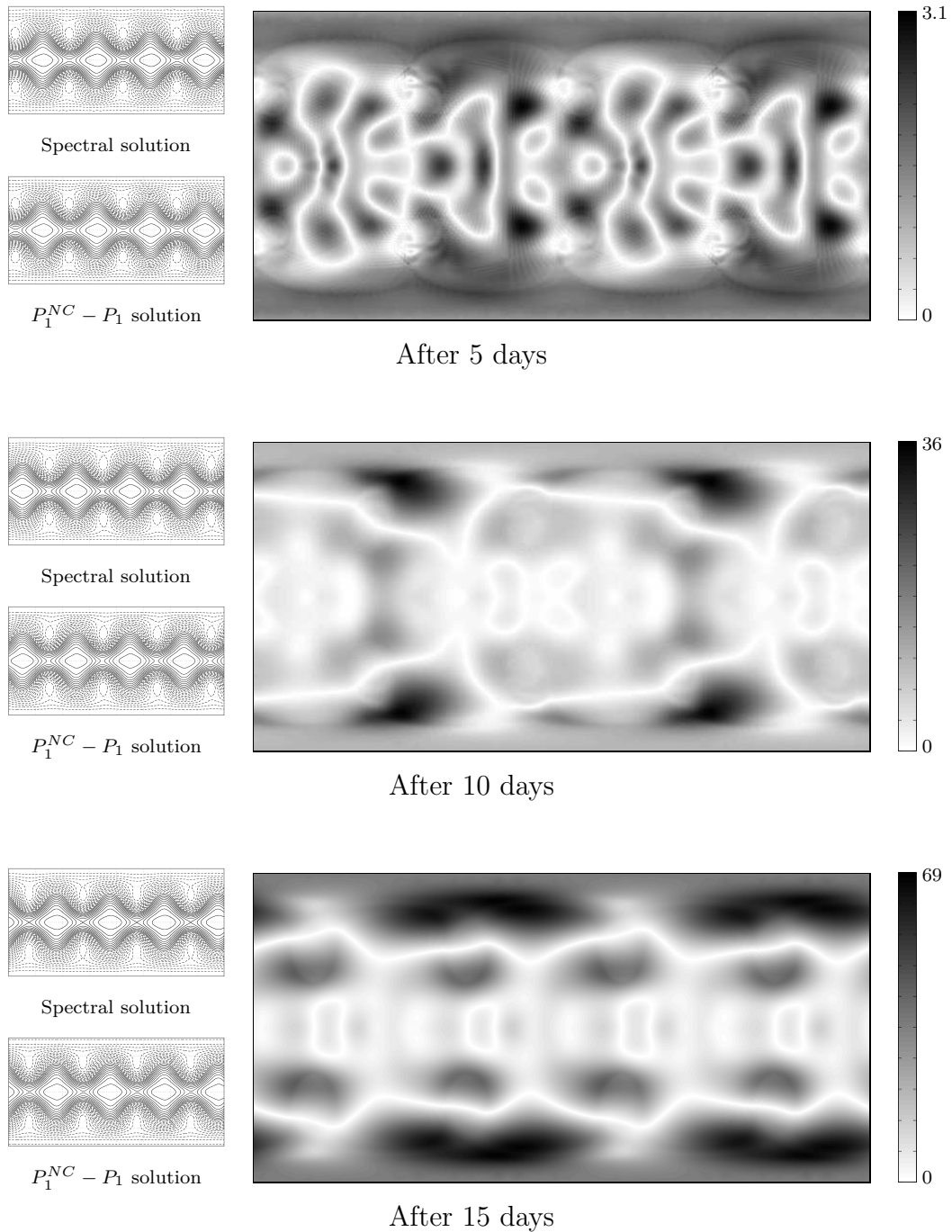


Figure 9. Comparison of the elevation field with reference solution from the German Weather Service for test case 6. The fields are presented in longitude-latitude projection. Left panel: spectral solution on top, and finite element solution on bottom. The interval between contourlines is 50m, the dashed lines are contourlines under the mean level, and the solid lines are contourlines above the mean level. Right panel: visualization of the absolute value of the difference between the reference solution and the finite element solution. The colormaps for the difference ranges in  $[0; 3.1]$ ,  $[0; 36]$  and  $[0; 69]$  (white is 0, black is maximum).

## 4 Perturbed Rossby-Haurwitz waves

As the Rossby-Haurwitz flow of W92 is unstable to small perturbations (Thuburn and Li, 2000), Smith and Dritschel (2006) proposed a small variation of it, so that the instability is initially excited, and the numerical methods behave in a deterministic way. A small perturbation is added to the initial elevation field. This perturbation is defined as :

$$H \frac{(xx_0 + yy_0 + zz_0)}{40r^2}, \quad (19)$$

with  $H$  the mean fluid height (i.e. 9523 m),  $(x, y, z)$  the coordinates of the point in the global Cartesian frame of reference with origin at the center of the sphere,  $(x_0, y_0, z_0)$  a specific point located at latitude 40°North and longitude 50°East, and  $r$  is the radius of the Earth.

The advantage of this test case over its W92 counterpart is that it is reproducible: Thuburn and Li (2000) showed that for the classical Rossby-Haurwitz test case, the flow is unstable, and thus the behavior of the simulation is completely dependent on the way the numerical scheme excites the unstable mode(s).

Figure 10 compares our solution to that of Smith and Dritschel (2006), who used a contour-advective semi-Lagrangian method on a 256x256 grid, with a 108 s time-step. By contrast, our simulation was carried out with the same configuration as for initial Rossby-Haurwitz waves test case, i.e. with the icosahedral grid refined six times and a 60 s time-step. The flow pattern is relatively well represented, but the difference with respect to the reference solution is not negligible (the maximum differences after 5, 10 and 15 days are respectively 42, 147 and 221 m). This is probably due to a bias either in the reference solution or in our initial condition. To ensure that our method converges to a unique solution, we have considered as exact solution the result of a simulation carried out on the icosahedral mesh refined seven times (counting 327680 triangles), and observed how scalar diagnostics converge. This is illustrated in figure 11. We see that the maximum and minimum values of elevation converge both at an acceptable rate. Further, the error on the total energy of the system after fifteen days, illustrated in figure 12, converges at a higher rate than expected.

## 5 Conclusions

In this article, we propose an original solution for solving PDEs on the sphere — or on any other curved manifold. Taking advantage of the geometrical

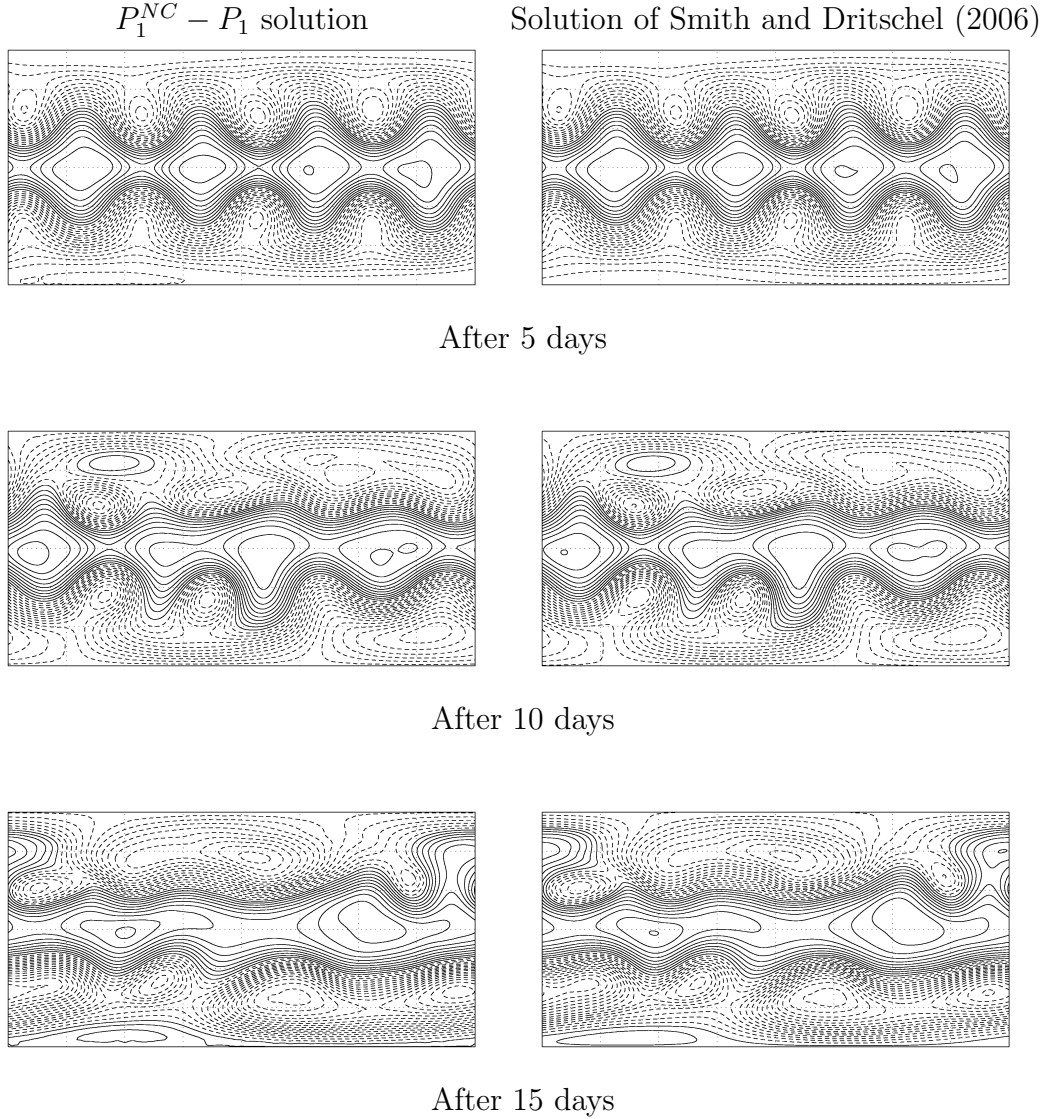


Figure 10. Comparison of the results for the modified Rossby-Haurwitz waves test case. The fields are presented in longitude-latitude projection. Reference solution of Smith and Dritschel (2006) (left) and our finite element solution (right). The interval between contourlines is 100m, the dashed lines are contourlines under the mean level, and the solid lines are contourlines above the mean level.

flexibility inherent to the finite element method, the presented methodology consists in a clever dialogue between a local and a nodal coordinate systems. As all elements are handled in the same way, the pole singularity issues are completely circumvented.

In order to assess the methodology, we show how to easily convert a finite element code operational in planar geometry into an efficient PDEs solver in spherical geometry, with a very small computational overhead. We prove that this new solver is able to reproduce accurately the solutions of the traditional

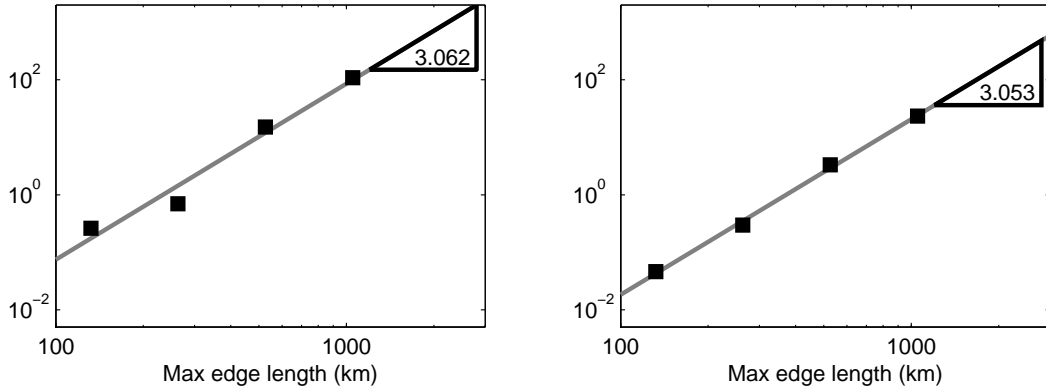


Figure 11. Convergence of the difference between reference solution and finite element solution for minimum (left) and maximum (right) values of elevation for perturbed Rossby-Haurwitz waves test case after five days.

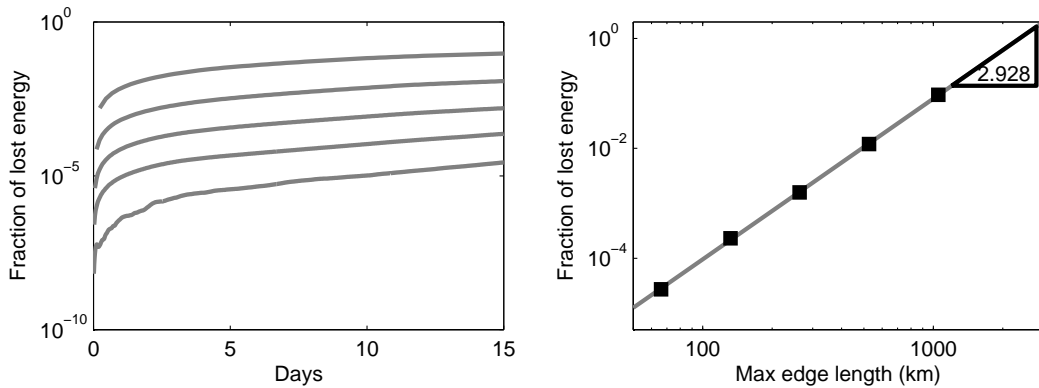


Figure 12. Fraction of total energy lost by the scheme for perturbed Rossby-Haurwitz waves test case. Left: time series for the four meshes, right: convergence after 15 physical days.

test case flows for the shallow water equations. We observe optimal rates of convergence on both elevation and velocity fields on steady state flows, as well as on different diagnostics for unsteady flows. Our solution of complex flows compares well with published results.

If the article mainly focuses on two-dimensional horizontal flows, the extension the three-dimensional case is rather straightforward. As explained by White et al. (2008b,a), our three-dimensional finite element model uses prisms as three-dimensional elementary unit. They are obtained by vertically extruding a two-dimensional triangular mesh. Section 2 showed that all the integrals are computed in the local coordinate system  $\mathbf{e}_\xi$ ,  $\mathbf{e}_\eta$ ,  $\mathbf{e}_\zeta$ . If the extrusion of the mesh is realized in the local coordinate system, aligned with the local vertical direction  $\mathbf{e}_\zeta$ , all the previous considerations are valid, if we consider the three-dimensional vector quantity as the combination of a two-dimensional vector tangent to the surface with a scalar value, which is its normal component. Note that we have implicitly assumed that we deal with a thin layer of fluid,

since the extrusion is achieved along a constant direction within the triangle (parallel extrusion), rather than extrusion toward the center of the sphere.

## **Acknowledgments**

Richard Comblen and Eric Deleersnijder are Research fellow and Research associate, respectively, with the Belgian National Fund for Scientific Research (FNRS). The present study was carried out within the scope of the project "A second-generation model of the ocean system", which is funded by the Communauté Française de Belgique, as Actions de Recherche Concertées, under contract ARC 04/09-316.

## A Scaling of second kind Christoffel symbols

Consider a sphere of radius  $r$ . For each flat triangle, we define a local cartesian basis  $\mathbf{e}_\xi, \mathbf{e}_\eta, \mathbf{e}_\zeta$ , with  $\mathbf{e}_\xi$  and  $\mathbf{e}_\eta$  parallel to the plane of the triangle. To make the derivation of metric terms easier, the origin of this cartesian basis is the center of the sphere. There exists an isomorphism  $\mathbf{x}(\boldsymbol{\xi})$  transforming the flat triangle into the spherical triangle (as illustrated in figure A.1):

$$\mathbf{x}(\boldsymbol{\xi}) = \frac{r}{\|\boldsymbol{\xi}\|} \boldsymbol{\xi}. \quad (\text{A.1})$$

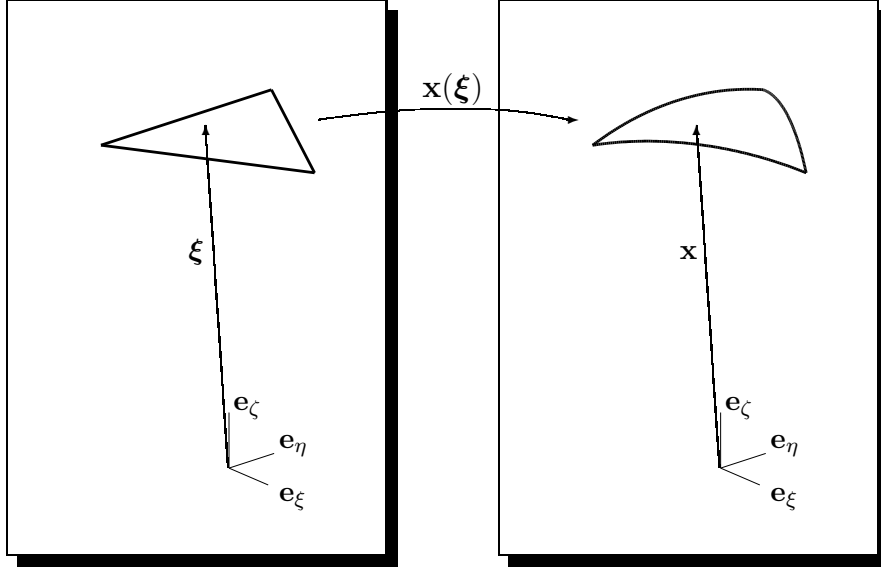


Figure A.1. The isomorphism turning a flat triangle into a spherical one.

Using this isomorphism, we can deduce the covariant basis of the spherical triangle:

$$\begin{aligned} \mathbf{g}_\xi &= \frac{\partial \mathbf{x}(\boldsymbol{\xi})}{\partial \xi} = \frac{r}{\|\boldsymbol{\xi}\|} \left( \mathbf{e}_\xi - \xi \frac{\boldsymbol{\xi}}{\|\boldsymbol{\xi}\|^2} \right), \\ \mathbf{g}_\eta &= \frac{\partial \mathbf{x}(\boldsymbol{\xi})}{\partial \eta} = \frac{r}{\|\boldsymbol{\xi}\|} \left( \mathbf{e}_\eta - \eta \frac{\boldsymbol{\xi}}{\|\boldsymbol{\xi}\|^2} \right), \\ \mathbf{g}_\zeta &= \frac{\boldsymbol{\xi}}{\|\boldsymbol{\xi}\|}. \end{aligned}$$

In the case of a curved surface embedded into the three-dimensional space, the second kind Christoffel symbols  $\Gamma_{\alpha\beta}^\gamma$  (with  $\alpha, \beta$ , and  $\gamma$  being  $\xi$  or  $\eta$ ) can be computed from:

$$\frac{\partial \mathbf{g}_\alpha}{\partial \beta} = \sum_{\gamma=\xi,\eta} \Gamma_{\alpha\beta}^\gamma \mathbf{g}_\gamma + n_{\alpha\beta} \mathbf{g}_\zeta, \quad (\text{A.2})$$

where  $n_{\alpha\beta}$  are coefficient that need not to be computed, as they are related to the component normal to the surface. For our specific application, this leads to:

$$\begin{aligned} \Gamma_{\xi\xi}^\xi &= -2 \frac{\xi}{\|\boldsymbol{\xi}\|^2}, & \Gamma_{\xi\eta}^\xi &= \Gamma_{\eta\xi}^\xi = \frac{\eta}{\|\boldsymbol{\xi}\|^2}, & \Gamma_{\eta\eta}^\xi &= 0, \\ \Gamma_{\xi\xi}^\eta &= 0, & \Gamma_{\xi\eta}^\eta &= \Gamma_{\eta\xi}^\eta = -\frac{\xi}{\|\boldsymbol{\xi}\|^2}, & \Gamma_{\eta\eta}^\eta &= -2 \frac{\eta}{\|\boldsymbol{\xi}\|^2}. \end{aligned}$$

Therefore, the estimation of the order of magnitude for these symbols is straightforward:

$$\begin{aligned} \xi &\in [0; h], \\ \|\boldsymbol{\xi}\| &= \sqrt{(r')^2 + \xi^2} \approx r, \\ \Gamma_{\alpha\beta}^\gamma &\approx \frac{h}{r^2}, \end{aligned}$$

for  $\alpha, \beta$  and  $\gamma$  being  $\xi$  or  $\eta$ . Of course, the asymptotic assumption  $h \ll r$  is always valid in ocean modeling.

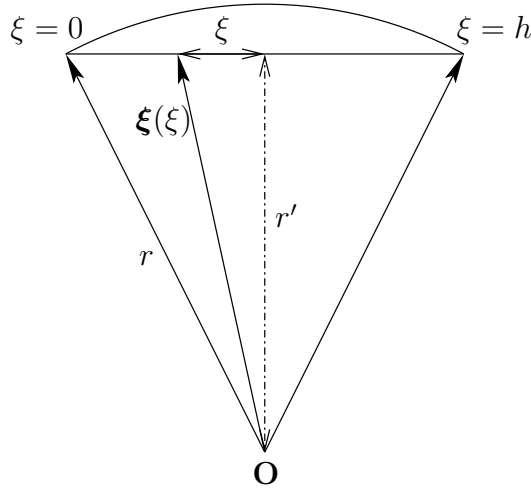


Figure A.2. A one-dimensional illustration of the different terms involved in the calculation of Christoffel symbols.

## References

- Adcroft, A., Campin, J.-M., Hill, C., Marshall, J., 2004. Implementation of an atmosphere-ocean general circulation model on the expanded spherical cube. *Monthly Weather Review* 134, 2845–2863.
- Ascher, U. M., Ruuth, S. J., Spiteri, R. J., 1997. Implicit-explicit Runge-Kutta methods for time-dependent partial differential equations. *Applied Numerical Mathematics* 25, 151–167.
- Blumberg, A. F., Mellor, G. L., 1987. A description of three-dimensional coastal ocean circulation model. In: Heaps, N. S. (Ed.), *Three Dimensional Coastal Ocean Model*. American Geophysical Union, pp. 1–16.
- Côté, J., 1988. A Lagrange multiplier approach for the metric terms of semi-Lagrangian models on the sphere. *Quarterly Journal of the Royal Meteorological Society* 114, 1347–1352.
- Coward, A. C., Killworth, P. D., Blundell, J. R., 1994. Tests of a two-grid world ocean model. *Journal of Geophysical Research* 99, 725–735.
- Deleersnijder, E., Campin, J.-M., 1995. On the computation of the barotropic mode of a free-surface world ocean model. *Annales Geophysicae* 13, 675–688.
- Deleersnijder, E., Van Ypersele, J.-P., Campin, J.-M., 1993. An orthogonal curvilinear coordinate system for a world ocean model. *Ocean Modelling (Newsletter)* 100, 7–10, (unpublished manuscript).
- Eby, M., Holloway, G., 1994. Grid transformation for incorporating the Arctic in a global ocean model. *Climate Dynamics* 10, 241–247.
- Gadd, A. J., 1978. A split-explicit integration scheme for numerical weather prediction. *Quarterly Journal of the Royal Meteorological Society* 104, 569–582.
- Giraldo, F. X., 2000. Lagrange-Galerkin methods on spherical geodesic grids : The shallow water equations. *Journal of Computational Physics* 160, 336–368.
- Giraldo, F. X., 2006. High-order triangle-based discontinuous Galerkin methods for hyperbolic equations on a rotating sphere. *Journal of Computational Physics* 214, 447–465.
- Giraldo, F. X., Hesthaven, J. S., Warburton, T., 2002. Nodal high-order discontinuous Galerkin methods for the spherical shallow water equations. *Journal of Computational Physics* 181, 499–525.
- Giraldo, F. X., Perot, J. B., Fischer, P. F., 2003. A spectral element semi-lagrangian (SESL) method for the spherical shallow water equations. *Journal of Computational Physics* 190, 623–650.
- Giraldo, F. X., Warburton, T., 2005. A nodal triangle-based spectral element method for the shallow water equations on the sphere. *Journal of Computational Physics* 207, 129–150.
- Gresho, P. M., Sani, R. L., 2000. *Incompressible Flow and the Finite Element Method - Isothermal Laminar Flow*. Wiley.
- Hallberg, R., 1997. Stable split time stepping schemes for large-scale ocean modeling. *Journal of Computational Physics* 135, 54–56.

- Hanert, E., Legat, V., 2006. How to save a bad element with weak boundary conditions. *Computer & Fluids* 35, 477–484.
- Hanert, E., Roux, D. L., Legat, V., Deleersnijder, E., 2004. Advection schemes for unstructured grid ocean modelling. *Ocean Modelling* 7, 39–58.
- Hanert, E., Roux, D. Y. L., Legat, V., Deleersnijder, E., 2005. An efficient eulerian finite element method for the shallow water equations. *Ocean Modelling* 10, 115–136.
- Haurwitz, B., 1940. The motion of atmospheric disturbances on the spherical earth. *Journal of Marine Research* 3, 254–267.
- Heikes, R., Randall, D. A., 1995. Numerical integration of the shallow-water equations on a twisted icosahedral grid. part i: Basic design and results of tests. *Monthly Weather Review* 123, 1862–1880.
- Higdon, R. L., 2002. A two-level time-stepping method for layered ocean circulation models. *Journal of Computational Physics* 177, 59–94.
- Higdon, R. L., de Szoeke, R. A., 1997. Barotropic-baroclinic time splitting for ocean circulation modeling. *Journal of Computational Physics* 135, 30–53.
- Hughes, T. J., 2000. *The Finite Element Method - Linear Static and Dynamic Finite Element Analysis*. Dover.
- Jakob-Chien, R., Hack, J. J., Williamson, D. L., 1995. Spectral transform solutions to the shallow water test set. *Journal of Computational Physics* 119, 164–287.
- Killworth, P. D., Stainforth, D., Webb, D. J., Paterson, S. M., september 1991. The development of a free-surface Bryan-Cox-Semtner ocean model. *Journal of Physical Oceanography* 21, 1333–1348.
- Lanser, D., Blom, J. G., Verwer, J. G., 2000. Spatial discretization of the shallow water equations in spherical geometry using Osher’s scheme. *Journal of Computational Physics* 165, 542–565.
- Le Roux, D. Y., Sene, A., Rostand, V., Hanert, E., 2005. On some spurious mode issues in shallow-water models using a linear algebra approach. *Ocean Modelling* 10, 83–94.
- Madala, R. V., 1981. Efficient time integration schemes for atmosphere and ocean models. In: Book, D. L. (Ed.), *Finite-difference techniques for vectorized fluid dynamics calculations*. Springer, Heidelberg.
- Madec, G., Imbard, M., 1996. A global ocean mesh to overcome the North Pole singularity. *Climate Dynamics* 12, 381–388.
- Majewski, D., Liermann, D., Prohl, P., Ritter, B., Buchhold, M., Hanisch, T., Paul, G., Wergen, W., Baumgardner, J., 2002. The operational global icosahedral-hexagonal gridpoint model gme : Description and high-resolution tests. *Monthly Weather Review* 130, 319–338.
- Murray, R. J., 1996. Explicit generation of orthogonal grids for ocean models. *Journal of Computational Physics* 126, 251–273.
- Murray, R. J., Reason, C. J. C., 2002. Fourier filtering and coefficient tapering at the North Pole in OGCMs. *Ocean Modelling* 4, 1–25.
- Nair, R. D., Thomas, S. J., Loft, R. D., 2005. A discontinuous Galerkin global shallow water model. *Monthly Weather Review* 133, 876–888.

- Priestley, A., 1992. The Taylor-Galerkin method for the shallow-water equations on the sphere. *Monthly Weather Review* 120, 3003–3015.
- Roberts, J. L., Heil, P., Murray, R. J., Holloway, D. S., Bindoff, N. L., 2006. Pole relocation for an orthogonal grid: an analytic method. *Ocean Modelling* 12, 16–31.
- Ronchi, C., Iacono, R., Paolucci, P. S., 1996. The "cubed sphere" : a new method for the solution of partial differential equations in spherical geometry. *Journal of Computational Physics* 124, 93–114.
- Rossmannith, J. A., 2006. A wave propagation method for hyperbolic systems on the sphere. *Journal of Computational Physics* 213, 629–658.
- Sadourny, R., Arakawa, A., Mintz, Y., 1968. Integration of the nondivergent barotropic vorticity equation with and icosahedral-hexagonal grid for the sphere. *Monthly Weather Review* 96, 351–356.
- Smith, R. K., Dritschel, D. G., 2006. Revisiting the Rossby-Haurwitz wave test case with contour advection. *Journal of Computational Physics* 217, 473–484.
- St-Cyr, A., Jablonowski, C., Dennis, J. M., Tufo, H. M., Thomas, S. J., 2008. A comparison of two shallow water models with non-conforming adaptive grids. *Monthly Weather Review*, in press.
- Stuhne, G. R., Peltier, W. R., 1999. New icosahedral grid-point discretizations of the shallow water equations on the sphere. *Journal of Computational Physics* 148, 23–58.
- Stuhne, G. R., Peltier, W. R., 2006. A robust unstructured grid discretization for 3-dimensional hydrostatic flows in spherical geometry: A new numerical structure for ocean general circulation modeling. *Journal of Computational Physics* 213, 704–729.
- Swarztrauber, P. N., 1996. Spectral transform methods for solving the shallow-water equations on the sphere. *Monthly Weather Review* 124, 730–744.
- Swarztrauber, P. N., Williamson, D. L., Drake, J. B., 1997. The Cartesian method for solving partial differential equations in spherical geometry. *Dynamics of Atmospheres and Oceans* 27, 679–706.
- Taylor, M., Tribbia, J., Iskandarani, M., 1997. The spectral element method for the shallow water equations on the sphere. *Journal of Computational Physics* 130, 92–108.
- Thuburn, J., 1997. A PV-based shallow-water model on a hexagonal-icosahedral grid. *Monthly Weather Review* 125, 2328–2347.
- Thuburn, J., Li, Y., 2000. Numerical simulations of Rossby-Haurwitz waves. *Tellus* 52A, 181–189.
- Tomita, H., Tsugawa, M., Satoh, M., Goto, K., 2001. Shallow water model on a modified icosahedral geodesic grid by using spring dynamics. *Journal of Computational Physics* 174, 579–613.
- Webb, D., de Cuevas, B., Coward, A., 1998. The first main run of the OCCAM global ocean model. Internal document no. 34, Southampton Oceanography Centre.
- White, L., Deleersnijder, E., Legat, V., 2008a. A three-dimensional unstruc-

- tured mesh finite element shallow-water model, with application to the flows around an island and in a wind-driven elongated basin. *Ocean Modelling*, in press, doi:10.1016/j.ocemod.2008.01.001.
- White, L., Legat, V., Deleersnijder, E., 2008b. Tracer conservation for three-dimensional, finite-element, free-surface, ocean modeling on moving prismatic meshes. *Monthly Weather Review* 136, 420–442.
- Williamson, D. L., Drake, J. B., Hack, J. J., Jakob, R., Swarztrauber, P. N., 1992. A standard test set for numerical approximations to the shallow water equations in spherical geometry. *Journal of Computational Physics* 102, 211–224.